

## The influence of projection angle on nappe stability at low energy heads over the weir crest

Mohanad A. Khodier<sup>a,\*</sup> and Blake P. Tullis<sup>b</sup>

<sup>a</sup> Department of Civil Engineering, Yarmouk University, P. O. Box 566, Irbid, Jordan

<sup>b</sup> Utah Water Research Laboratory, Department of Civil and Environmental Engineering, Utah State University, 8200 Old Main Hill, Logan, UT 84322-8200, USA

\*Corresponding author. E-mail: mohanad.khodier@yu.edu.jo

 MAK, 0000-0003-2510-1732

### ABSTRACT

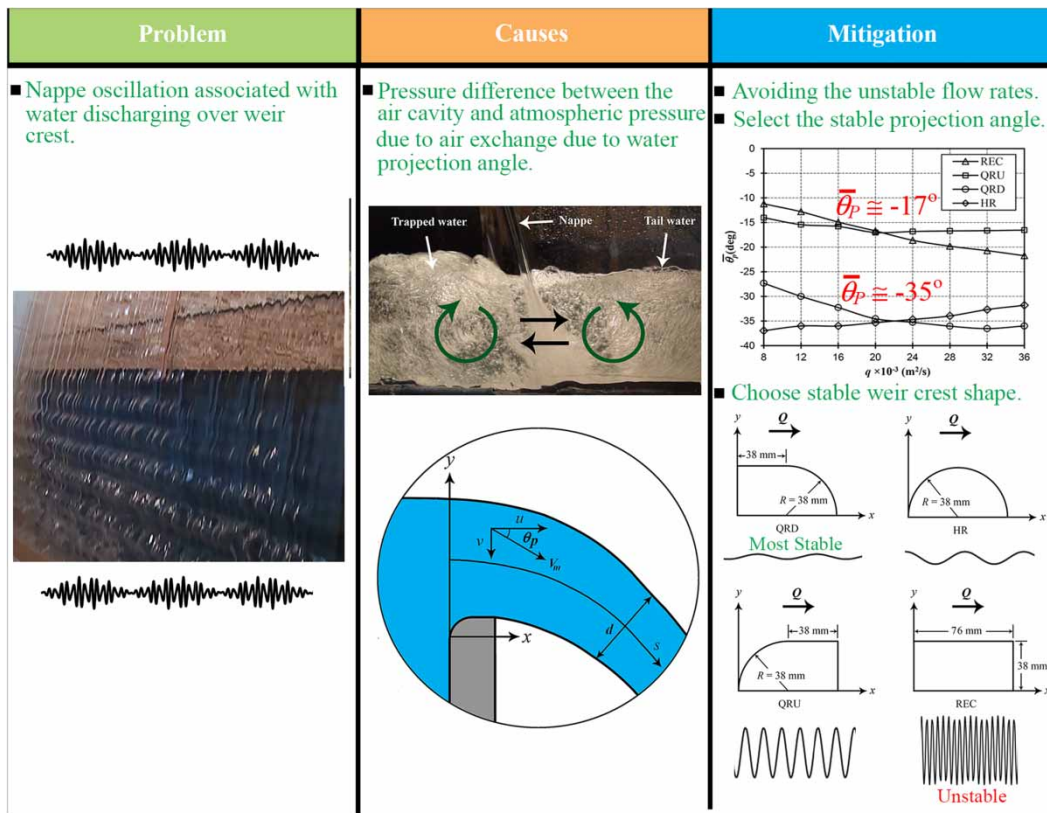
Under certain low head hydraulic conditions, weir discharge under gravity flow can produce an oscillating nappe characterized by horizontal waves and audible low-frequency acoustic energy, which in some cases can have a significant impact on the local environment. In an effort to better understand the mechanism behind nappe oscillation, an experimental investigation was conducted using a linear weir (1.83 m wide, 1.10 m in height, and 0.076 m in thickness) with four different crest shapes (rectangular, quarter-round upstream, half-round, and quarter-round downstream) at a wide range of unit discharge ranging from  $8 \times 10^{-3} \text{ m}^2/\text{s}$  to  $36 \times 10^{-3} \text{ m}^2/\text{s}$ . Using Particle Image Velocimetry (PIV) techniques, differential pressure measurements, and water surface profiles, the influence of Weber number, angle at which the nappe hits the downstream pool (angle of impact), and nappe projection angle on the nappe oscillation are reported. No significant relationship was found between the Weber number and nappe instability. The results suggest that the nappe is stable for unit discharge between  $20 \times 10^{-3}$  and  $24 \times 10^{-3} \text{ m}^2/\text{s}$  regardless the shape of the weir crest. Also, the stable projection angle is  $-17^\circ$  for rectangular and quarter-round upstream weirs and  $-35^\circ$  for half-round and quarter-round downstream weirs for the specific tested weir.

**Key words:** nappe, particle Image velocimetry (PIV), pressure, unaerated, vibration, Weber number

### HIGHLIGHTS

- Explain the mechanism behind the nappe oscillation precisely.
- Discover different types of nappe oscillation.
- Propose some mitigation solutions for nappe oscillation.
- Help designers choose the appropriate crest shape for nappe stability.
- Provide a solution for the existing dams that suffer from nappe oscillation.

## GRAPHICAL ABSTRACT



## NOTATION

$d$	the thickness of the nappe (m)
$f$	nappe oscillation frequency (Hz)
$h$	the upstream flow depth measured relative to the weir crest elevation (m)
$H$	$h + V^2/2g$ = total upstream head (m); $L$ = length of the weir (m)
$n$	number of collected data for the velocity across the nappe
$q$	unit discharge ( $\text{m}^2/\text{s}$ )
$Q$	flow rate ( $\text{m}^3/\text{s}$ )
$P$	the weir height (m)
$S$	the length of the path along the center of the nappe (m)
$u$	the time-averaged velocity in the $x$ -direction (m/s)
$v$	the time-averaged velocity in the $y$ -direction (m/s)
$V$	the average cross-sectional velocity upstream of the crest weir (m/s)
$V_m$	the velocity magnitude ( $\sqrt{u^2 + v^2}$ ) (m/s)
$\overline{(V_m)}$	the average of the velocity magnitude across the nappe (m/s)
$W$	Weber number (m/m); $x$ = $x$ -direction (m/s)
$y$	$y$ -direction (m/s)
$Z_c$	confidence coefficient and equals to 1.96 for 95% confidence level
$\Delta p$	the air differential pressure between the trapped air and the ambient air (pa)
$\Delta x$	the maximum nappe horizontal displacement (m)
$\varepsilon$	uncertainty in PIV velocity measurements (m/s)
$\theta_I$	the angle at which the nappe hits the tailwater (degree)
$\theta_p$	the projection angle of nappe when leaving the crest (degree)
$\overline{(\theta_p)}$	the average of the projection angle of nappe across the nappe (degree)
$\rho$	water density ( $\text{kg}/\text{m}^3$ )
$\mu$	mean velocity for $N$ sample (m/s)
$\sigma$	surface tension (N/m)
$\sigma_{SD}$	standard deviation for the PIV velocity measurement (m/s)

## INTRODUCTION

Weirs are hydraulic structures that are commonly used in open channel flow as flow control structures, flow measurement, and flow diversion. With gravity as the driving force, water flow passes over the weir creating a jet like structure referred to as a nappe (Crookston & Tullis 2012b). Under certain ambiguous hydraulic conditions, the nappe can become unstable and reveal oscillation behavior characterized with a wavy longitudinal nappe profile (Barlow *et al.* 2010; Lodomez *et al.* 2016, 2018b; Khodier & Tullis 2017; Kitsikoudis *et al.* 2021). The undesirable behaviors of nappe oscillation can induce a vibration in the hydraulic structure, which could be potentially dangerous if the frequency of the nappe oscillation equals that one of the structure (Lodomez *et al.* 2018a). Moreover, nappe oscillation can produce significant acoustic energy that can create an environmental nuisance near the structure (Crookston *et al.* 2014). Nappe oscillation behavior is not only limited to weir flow and it was also observed on fountains and gates.

The reason behind the occurrence of nappe oscillations is still not clearly identified although numerous studies (Barlow *et al.* 2010; De Rosa 2013) proposed theories trying to explain this phenomenon. Helmholtz instability theory describes a nappe instability mechanism associated with the shear force at the interface between two different fluids with different velocities and densities. Mori *et al.* (2012) performed an experimental study to investigate the relationship between the oscillation frequency of the vertical water sheet and the pressure fluctuation in the air chamber behind it. They observed that the pressure fluctuations frequency is identical to the frequency of the confined water sheet oscillations (between 5.3 and 17.4 Hz). They also analytically simulated the nappe oscillation behavior as a spring-mass system in which the air compressibility was considered as a spring and the water sheet was considered as the mass. The comparison of frequencies of the real experiment and the analytical mass-spring model showed that the frequency of analytical model was from 10 to 20 times larger than the frequency of the experiment results for unstable water sheets. A similar mass-spring model principle was reconsidered by a later study of De Rosa *et al.* (2014) but this time searching for nappe instability criteria. The flow was assumed one-dimensional, inviscid, without surface tension effect, and with a coordinate-type expansion for the flow variables. Utilizing the ansatz techniques, they found that the system is stable if the crossing time of a perturbation over the whole length of the domain is shorter than the period of the spring-mass oscillator and the resonance frequencies equaled one integer-plus-one-fourth times the frequency of the initial unstable nappe. An addition analytical mass-spring system was applied on nappe oscillations of a vertical thin sheet interaction with an air pocket in the presence of surface tension effect (Girfoglio *et al.* 2017). The physical analysis confirmed that the instability generated two propagation wave fronts both directed downstream if the flow is supercritical or one downstream wave if the flow is subcritical. No experimental validation was provided for their findings. Kyotoh (2002) studied the instability mechanisms of a falling water sheet with and without a confined air cavity. He concluded that the physical factors affecting the motion of falling water sheet are the propagation of the pressure fluctuations for the trapped air, the air shear wave instability, and water surface tension. No pressure data were presented in Kyotoh's study. Sato *et al.* (2007) studied experimentally and analytically the behavior of falling water sheets with a back wall. They concluded that some of the energy gained by the sheet while falling under gravity was converted into vibration energy. Also, they concluded that the frequency of the water sheet is the same as that of the pressure in the air trapped behind the water sheet but no experimental measurements for the pressure were included in their study. Schmid & Henningson (2002) derived a mathematical expression for the stability of a two-dimensional falling liquid sheet and compared the results with experimental data. They found that there was a good correlation between the frequencies obtained by their model and the experimentally observed frequencies.

Physical modeling of hydraulic structures has been a powerful engineering bridge to transform hydraulic quantities between the field-scale prototype flow behavior and laboratory-scale models. The similitude principle is based on dimensionless numbers such as Froude, Reynolds, Weber number, etc. Among them, the former is most appropriate for most weir flow applications as it characterizes the interaction between gravity and inertia forces. However, under certain hydraulic conditions, Froude number similitude can result in differences between the prototype and the model, a condition referred to as scale effects (Heller 2011). The accuracy of simulating the nappe oscillation behavior at the prototype and model scales using Froude number similitude was studied experimentally by Anderson & Tullis (2018). Although they observed the nappe oscillation in prototype- and laboratory-scale models, discrepancies in the frequencies and oscillation behavior between the model and prototype was observed, leading a conclusion that nappe oscillation is a unit discharge phenomenon and not a Froude-scalable phenomenon. Similar findings were reported by Lodomez *et al.* (2019b).

Recognizing the potential risk nappe oscillation occurrence in field hydraulic structures could produce, it's important to find practical solutions for eliminating this phenomenon. One effective mitigation technique is installing flow splitters to the gate or weir crest at curtain spacing in order to provide more ventilation for the air chamber behind the nappe (Anderson 2014). There are limitations for the splitter spacing to be avoided (less than 1 m) to prevent the occurrence of Görtler vortices in the boundary layer. Moreover, the installation of splitter may collect debris and other floating materials which could result in other hydraulic challenges (Crookston & Tullis 2012a; Lodomez *et al.* 2019a). Another mitigation technique is adding surface roughness to the weir crest for confined and unconfined nappe (Anderson & Tullis 2018). It was observed that increasing the nappe roughness was effective in eliminating nappe oscillation but only for unconfined nappe. Lodomez *et al.* (2019a) tested three mitigation solutions (elements added to the crest profile): 12 configurations with projecting elements, five configurations with deflectors, and one configuration with a step. Among the three mitigations, deflectors or a step produced the maximum noise reduction and resulted in a 3% reduction in the discharge coefficient.

Recently, Kitsikoudis *et al.* (2021) observed that the occurrence of nappe oscillation is associated with low velocity (low unit discharges ranging from 0.01 to 0.06 m<sup>2</sup>/s), regardless of the model scale. Since that the Froude number was unable to represent the nappe oscillation frequencies between weirs of differing sizes or scale, they derived a dimensionless nappe oscillation frequency expressed as a power function that correlated the fall height and the water depth at the point of detachment at the crest, for quarter-round and truncated half-round weir crests.

The goal of this paper is to describe the behavior of the nappe oscillation at different flow rates and for different weir crest shapes including rectangular (REC), quarter-round downstream (QRD), quarter-round upstream (QRU), and half-round (HR) crests. The influence of the weir crest shape on the nappe oscillation was reported. Also, the mechanism behind the nappe oscillation was explained using differential pressure measurements between the trapped air behind the nappe and the ambient, Weber number, the angle of the nappe projection downstream the crest, nappe trajectory profile, and velocity profiles distributions.

## EXPERIMENTAL SETUP

All experiments were conducted at Utah Water Research Laboratory (UWRL) at Utah State University. The nappe was created in a flume 9 m long, 1.83 m wide, and 1.22 m in height as shown in Figure 1. The flume was supplied with water via a pipe of 0.50 m in diameter. At 0.40 m from the supply pipe outlet, a flow straightening (honeycomb) was placed to straighten the flow and reduce the flow turbulence before being discharged through the weir. A venturi flow meter of  $\pm 0.25\%$  accuracy was used to measure the flow rates. The upstream flow depth was measured using a precision point gauge installed upstream of the weir (5 m from the upstream of the weir) and referenced to the crest elevation. A wooden weir of 1.83 m wide, 1.10 m in height, and 0.076 m thick was used to generate a free-falling nappe. To provide support for the wooden weir, internal steel beams were used to reinforce the weir. The weir crest was made from high-density polyethylene (HDPE). Four different

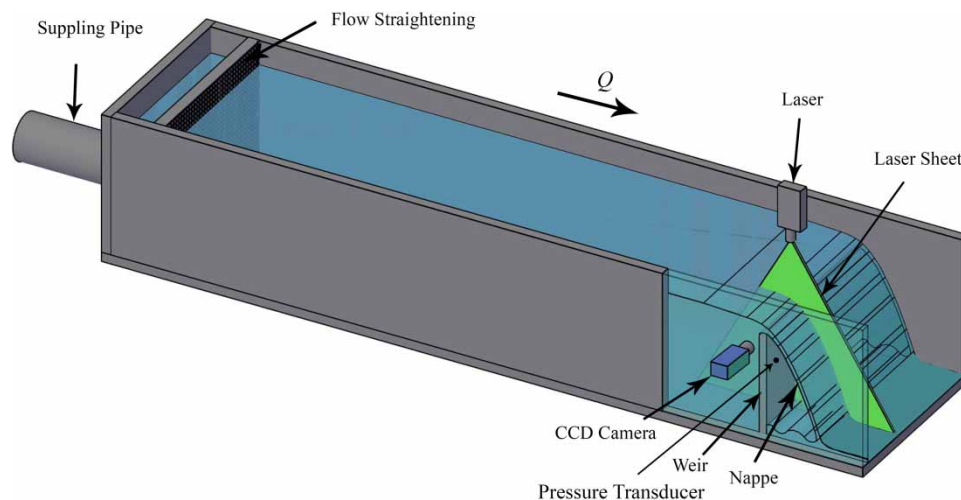


**Figure 1** | Schematic of the flume facilities.

weir crest shapes were used in this experiment including the REC, QRU, HR, and QRD as shown in Figure 2. The free-falling nappe was surrounded by the flume walls to prevent the air exchange between the trapped air behind the nappe and the surrounding air (unaerated nappe). A differential pressure transducer ( $\pm 1\%$  accuracy), located as shown in Figure 1, was used to measure the pressure difference between the trapped air behind the nappe and the local atmospheric pressure. A digital protractor ( $\pm 0.1^\circ$  accuracy) was used to measure angles when needed. A clear acrylic wall of  $2.44 \text{ m} \times 1.22 \text{ m}$  was installed near the weir wall location on both sides of the flume to provide a clean scene for the nappe trajectory profiles and for the Particle Image Velocimetry (PIV) instruments that were used to collect the velocity field measurements. Neutrally buoyant hollow micro-spherical glass particles of  $10 \mu\text{m}$  in diameter and a density of  $1.10 \pm 0.05 \text{ g/cc}$  were used to seed the flow. A frequency-doubled pulsed Nd: YAG (neodymium-doped yttrium-aluminum-garnet) laser of  $532 \text{ nm}$  wavelength was used to illuminate the flow field. All the velocity measurements were recorded at  $30 \text{ cm}$  from the clear acrylic wall to eliminate the sidewall effect on the flow behavior. A CCD camera of  $1376 \times 1040$  pixels resolution which operated at  $15 \text{ Hz}$  was used to record the scattered light from the first and second exposure of the seeded particles. A lens of  $50 \text{ mm}$  which has a minimum  $f$ -number of  $1.8$  was fitted to the camera light sensor port (see Figure 1). The crest was coated with fluorescent paint to reduce the laser light reflection of the crest and improve the PIV image quality near the wall. A hundred instantaneous recorded images were recorded for each flow condition and processed using a cross-correlation for  $64 \times 64$  pixels (first pass) and  $32 \times 32$  pixels (second pass) interrogation windows (IW) with  $50\%$  overlap. The flow rates were presented in a unit discharge  $q$  ( $\text{m}^2/\text{s}$ ) which is obtained by dividing the actual flow rate  $Q$  ( $\text{m}^3/\text{s}$ ) by the weir length. For each weir crest shape, the experiments were performed at a wide range of flow rates ranging from  $8 \times 10^{-3} \text{ m}^2/\text{s}$  to  $36 \times 10^{-3} \text{ m}^2/\text{s}$  with  $4 \times 10^{-3} \text{ m}^2/\text{s}$  increment. The uncertainty for the mean velocity components measurement using the PIV device from  $N$  individual samples can be calculated per the following equation (Scarano & Riethmuller 1999):

$$\varepsilon = \frac{Z_c \cdot \sigma_{SD}}{\mu \cdot \sqrt{N}} \quad (1)$$

where  $Z_c$  is the confidence coefficient and equals to  $1.96$  for  $95\%$  confidence level,  $\sigma_{SD}$  is the standard deviation of the velocity, and  $\mu$  the mean velocity for  $N$  samples. The uncertainty for these velocity measurements was less than  $2\%$  and the uncertainty for sub-pixel displacement was  $0.1$  pixels (less than  $2.5\%$ ). Also, the nappe trajectory profiles ( $\pm 0.5 \text{ mm}$  uncertainty) measured at the lower surface of the nappe were reported for different weir shapes and at different flow conditions. The uncertainty of Weber number calculation for  $95\%$  confidence level is estimated to be less than  $4.2\%$  using the Taylor Series Method (TSM).

## EXPERIMENTAL RESULTS AND DISCUSSION

Table 1 summarizes the nappe status (oscillating/non-oscillating/clinging) and total energy head at each flow rate for different crest shapes. It can be shown from Table 1 that the nappe stability depends mainly on the flow rates and the crest shape. Also, note that the nappe created with the QRD is stable regardless of the flow condition. Table 2 summarizes the minimum and maximum differential pressure and frequency for different crest shapes and flow rates. As can be observed from Table 2, there is no clear relationship between the oscillation frequencies and the differential pressure for air cavity. The maximum

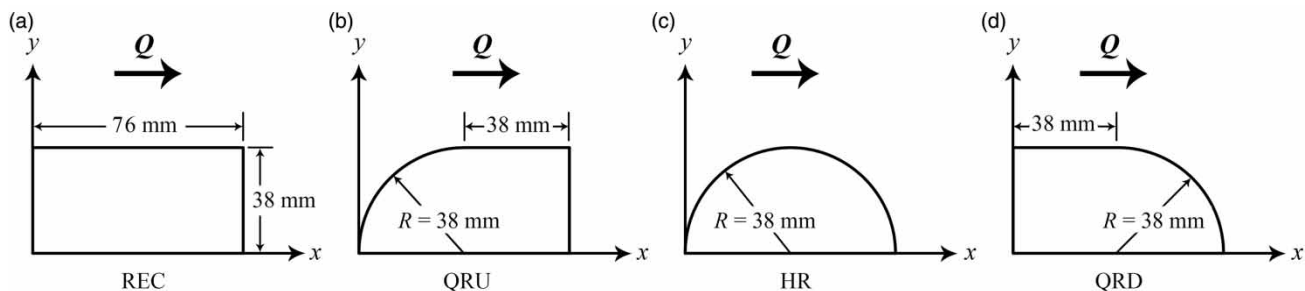


Figure 2 | Tested weir crest shapes.



**Table 1** | Summary of the nappe status and total energy head at different flow rates for different crest shapes

$q \times 10^{-3}$ (m <sup>2</sup> /s)	Crest shape			
	REC	QRU	HR	QRD
4.0	Oscillating ( $H=0.0183$ m)	Oscillating ( $H=0.0143$ m)	No nappe (clinging) ( $H=0.0159$ m)	No nappe (clinging) ( $H=0.0219$ m)
8.0	Oscillating ( $H=0.0293$ m)	Oscillating ( $H=0.0246$ m)	No nappe (clinging) ( $H=0.0253$ m)	No nappe (clinging) ( $H=0.0323$ m)
12.0	Oscillating ( $H=0.0387$ m)	Oscillating ( $H=0.0326$ m)	No nappe (clinging) ( $H=0.0323$ m)	No nappe (clinging) ( $H=0.0408$ m)
16.0	Oscillating ( $H=0.0466$ m)	Non-oscillating ( $H=0.0396$ m)	No perfect confined nappe ( $H=0.0387$ m)	No nappe (clinging) ( $H=0.0466$ m)
20.0	Non-oscillating ( $H=0.0537$ m)	Non-oscillating ( $H=0.0460$ m)	Non-oscillating ( $H=0.0442$ m)	No nappe (clinging) ( $H=0.0527$ m)
24.0	Oscillating ( $H=0.0604$ m)	Non-oscillating ( $H=0.0515$ m)	Non-oscillating ( $H=0.0494$ m)	No perfect confined nappe ( $H=0.0582$ m)
28.0	Oscillating ( $H=0.0659$ m)	Non-oscillating ( $H=0.0564$ m)	Non-oscillating ( $H=0.0540$ m)	No perfect confined nappe ( $H=0.0637$ m)
32.0	Oscillating ( $H=0.0741$ m)	Oscillating ( $H=0.0625$ m)	Oscillating ( $H=0.0592$ m)	No perfect confined nappe ( $H=0.0686$ m)
36.0	Oscillating ( $H=0.0772$ m)	Oscillating ( $H=0.0668$ m)	Oscillating ( $H=0.0638$ m)	Non-oscillating ( $H=0.0729$ m)

**Table 2** | Minimum and maximum differential pressure and frequencies at different flow rates and for different crest shapes

$q \times 10^{-3}$ (m <sup>2</sup> /s)	Crest shape							
	REC		QRU		HR		QRD	
	$\Delta P_{\min} - \Delta P_{\max}$ (Pa)	$f_{\min} - f_{\max}$ (Hz)	$\Delta P_{\min} - \Delta P_{\max}$ (Pa)	$f_{\min} - f_{\max}$ (Hz)	$\Delta P_{\min} - \Delta P_{\max}$ (Pa)	$f_{\min} - f_{\max}$ (Hz)	$\Delta P_{\min} - \Delta P_{\max}$ (Pa)	$f_{\min} - f_{\max}$ (Hz)
4.0	-6.1 to 2.7	N/A	-3.1 to 22.1	N/A	N/A	N/A	N/A	N/A
8.0	-5.6 to 3.2	N/A	-3.8 to 17.9	N/A	N/A	N/A	N/A	N/A
12.0	-5.3 to 4.8	53.3–60.1	-4.2 to 20.1	42.8–60.2	N/A	N/A	N/A	N/A
16.0	-5.5 to 4.8	54.3–63.8	-2.5 to 16.2	N/A	N/A	N/A	N/A	N/A
20.0	-6.2 to 4.0	N/A	N/A	N/A	N/A	N/A	N/A	N/A
24.0	-4.2 to 7.5	21.7–33.4	-8.5 to 7.2	N/A	N/A	N/A	N/A	N/A
28.0	-7.0 to 9.2	34.0–36.8	-23.6 to 10.2	N/A	N/A	N/A	N/A	N/A
32.0	-8.2 to 9.8	7.2–10.3	-53.2 to 16.8	31.5–38.2	-43.8 to 33.2	38.3–47.7	N/A	N/A
36.0	-9.4 to 9.7	8.3–12.5	-102.7 to 91.7	32.3–34.5	-96.3 to 88.2	34.7–35.6	N/A	N/A

differential pressure occurs at higher flow rates for QRU and HR crests. The nappe oscillating is discussed per the following parameters.

### Nappe trajectory profiles and differential pressure

The nappe trajectory profile for quarter-round upstream (QRU) is reported and plotted in [Figure 3\(a\)](#) at the low unit discharge of  $q=8 \times 10^{-3}$  m<sup>2</sup>/s. As shown in [Figure 3\(a\)](#), the volume of the trapped air behind the nappe increases over time until it reaches a maximum volume and then the nappe starts to vibrate for a certain period. The volume of the trapped air behind the nappe at the end of the oscillation decreases to a volume that is between the initial and the maximum volume of the trapped air. It should be noted that the initial nappe trajectory profile represents full aerated nappe. The historical differential pressure measurements are shown in [Figure 3\(b\)](#). The differential pressure ( $\Delta p$ ) is defined as the differential pressure between the trapped air behind the nappe and the ambient air pressure. A positive value of ( $\Delta p$ ) means that the pressure of the trapped air is higher than the ambient pressure. As shown in [Figure 3\(b\)](#), the differential pressure has

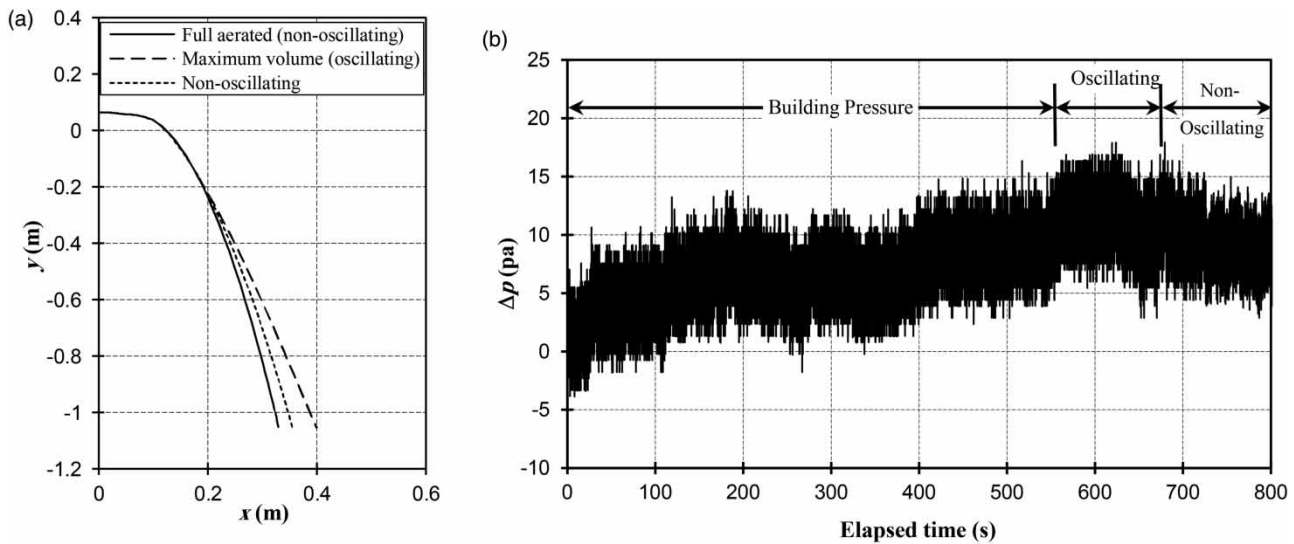


**Figure 3** | QRU at flow rate  $q = 8 \times 10^{-3} \text{ m}^2/\text{s}$ : (a) trajectory profile; (b) differential pressure.

three stages: the pressure building stage, oscillating stage, and non-oscillating stage. In the pressure building state, the pressure increases over time until it reaches the maximum differential pressure (at a time equal to 560 s approximately) at which the oscillating stage takes a place. The nappe vibrates for 110 s and then it becomes stable and the process repeats every 6 min. This mode of vibration is called increasing-pressure increasing-volume and is only noted for the quarter-round upstream crest at low flow rates ( $q \leq 16 \times 10^{-3} \text{ m}^2/\text{s}$ ). Note that the differential pressure data are fluctuating all the time.

The behavior of the nappe trajectory for the same crest shape (QRU) at the higher unit discharge of  $q = 36 \times 10^{-3} \text{ m}^2/\text{s}$  is shown in Figure 4(a). As shown in Figure 4(a), the nappe behaves differently from that one at lower flow rates. The nappe trajectory profile is shifted toward the weir wall and the volume of the trapped air behind the nappe decreases. Figure 4(b) shows the differential pressure measurements overtime for the QRU. When the nappe is fully aerated, the nappe is not oscillating and the differential pressure is fluctuating approximately around zero. For the unaerated nappe, the differential pressure increases but this time in the negative direction which means that the pressure of the trapped air goes below the atmospheric surrounding pressure. The differential pressure over time propagates more and more until it has higher

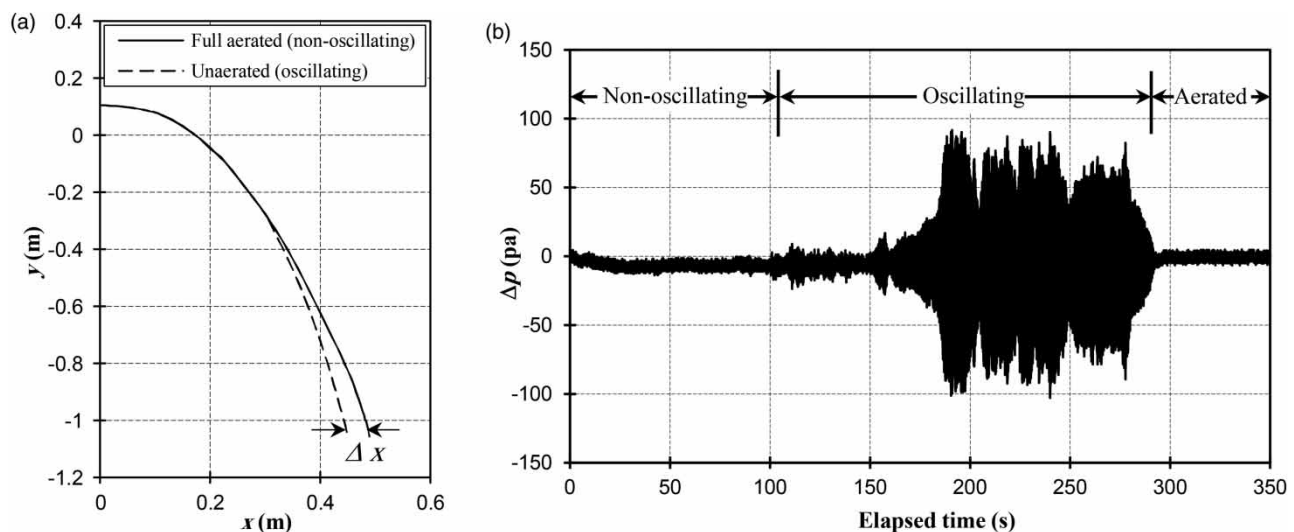


**Figure 4** | QRU at flow rate  $q = 36 \times 10^{-3} \text{ m}^2/\text{s}$ : (a) trajectory profile; (b) differential pressure.

amplitudes at which the vibration noise can be felt far away from the flume facilities in addition to the hard vibration in the flume structure. This type of nappe vibration was the hardest and noisiest one and it will be called decreasing-pressure decreasing-volume.

The nappe trajectory profile and the differential pressure data are presented in Figure 5 for the REC crest at the lower unit discharge of  $q = 8 \times 10^{-3} \text{ m}^2/\text{s}$ . Unlike the nappe behavior of the QRU at lower unit discharge, the nappe trajectory profile shifted back toward the weir wall when the nappe is unaerated as shown in Figure 5(a). The differential pressure data presented in Figure 5(b) show that the differential pressure fluctuates more in the negative direction with higher magnitudes when the nappe is unaerated. This type of vibration is harder than the vibration associated with QRU at low flow rates but smoother than that one of QRU at higher flow rates and can be classified under the decreasing-pressure decreasing-volume category. Also, the nappe trajectory profile and the differential pressure data are presented in Figure 6 for the REC crest at a higher unit discharge of  $q = 36 \times 10^{-3} \text{ m}^2/\text{s}$ . Note that the trajectory profile shifted back toward the weir wall when the nappe is unaerated and causes the differential pressure to fluctuate hardly (compared to the lower flow rate case) in the negative direction as shown in Figure 6(b). This type of vibration is not as hard as that one for the QRU at higher flow rates and occurs more frequently and happens as pulses that do not last more than a few seconds.

It was noted for the HR and QRD crest that there is no regular nappe produced at lower flow rates until a unit discharge of  $q = 20 \times 10^{-3} \text{ m}^2/\text{s}$ . For unit discharge less than  $q = 20 \times 10^{-3} \text{ m}^2/\text{s}$ , the nappe is clinging to the downstream of the weir. So, there are not any nappe trajectory data presented for these shapes of the crest at a unit discharge less than  $q = 20 \times 10^{-3} \text{ m}^2/\text{s}$  (see Table 1) and the nappe (if there is) is not oscillating. The nappe trajectory profile for HR crest at the unit discharge of  $q = 36 \times 10^{-3} \text{ m}^2/\text{s}$  is shown in Figure 7(a). The nappe trajectory profile is shifted back toward the weir wall when the nappe is unaerated. The vibration behavior for this crest shape is less hard than that of the QRU at high flow rates, doesn't last more than a few seconds, takes a long time to take place, and doesn't happen frequently. Compared to the REC crest, the nappe created with the HR crest at low flow rates is more stable than that one created with the HR at higher flow rates. For the QRD crest and at the higher unit discharge of  $q = 36 \times 10^{-3} \text{ m}^2/\text{s}$ , the nappe is self-aerated and there is no type of oscillation is reported for this crest shape over the entire range of the tested unit discharges. The nappe trajectory profile for the QRD crest is shown in Figure 7(b) at the unit discharge of  $q = 36 \times 10^{-3} \text{ m}^2/\text{s}$ . Note that the trajectory profile is different from other profiles and most of the profile is vertical and there is no change in the profile for the aerated and unaerated nappe.

### Maximum nappe trajectory displacement

The nappe displacement ( $\Delta x$ ) as a function of the unit discharge for different weir crest shapes is shown in Figure 8. The displacement ( $\Delta x$ ) is defined as the difference between the maximum horizontal point, measured from the downstream face of the weir wall, that the nappe can reach on the apron in the case of the aerated nappe and the final horizontal point that the

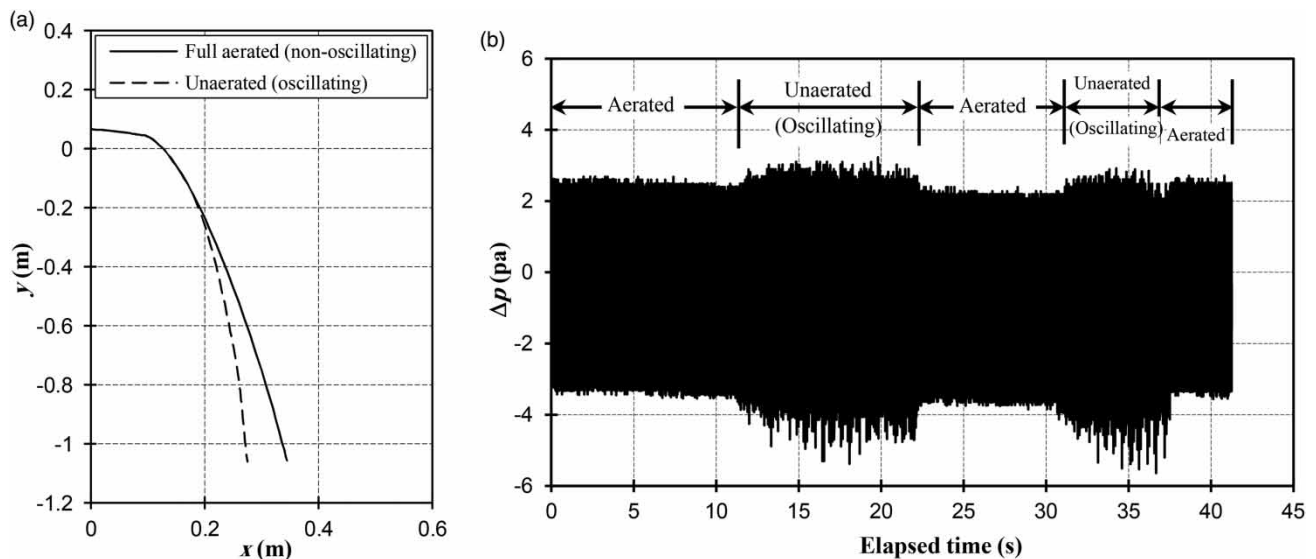


**Figure 5** | REC at flow rate  $q = 8 \times 10^{-3} \text{ m}^2/\text{s}$ : (a) trajectory profile; (b) differential pressure.



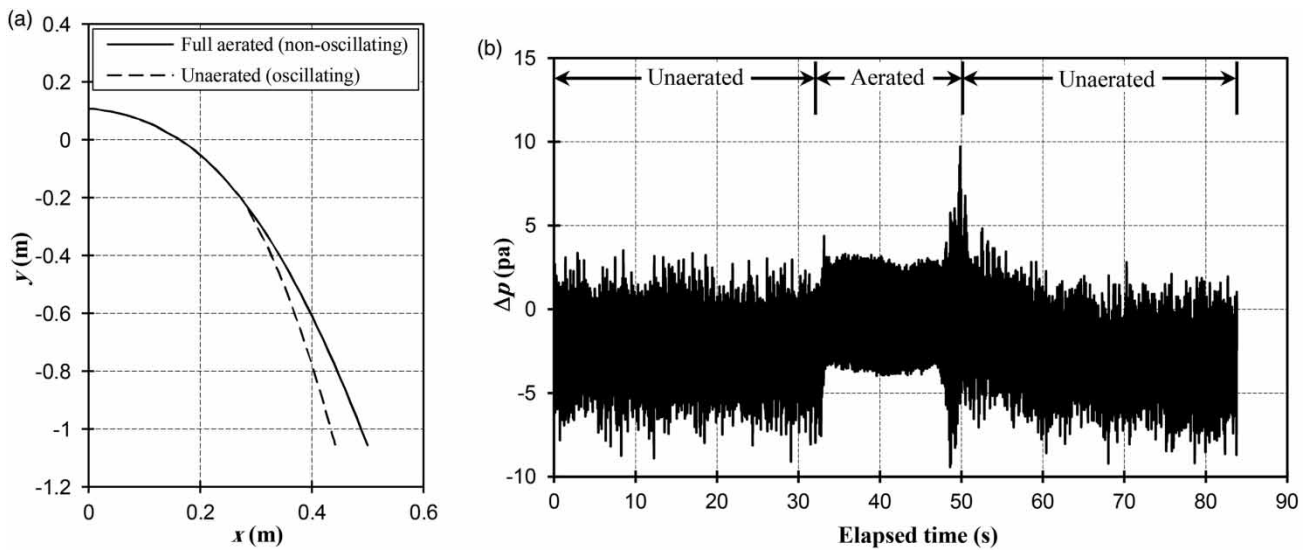


**Figure 6** | REC at flow rate  $q = 36 \times 10^{-3} \text{ m}^2/\text{s}$ : (a) trajectory profile; (b) differential pressure.

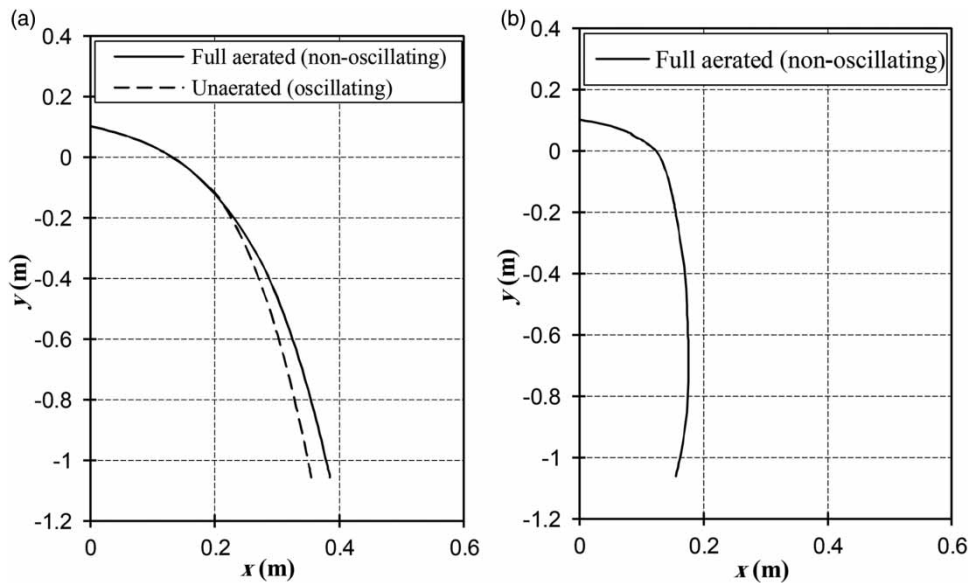


**Figure 7** | Trajectory profile at flow rate  $q = 36 \times 10^{-3} \text{ m}^2/\text{s}$ : (a) HR; (b) QRD.

nappe can reach in the case of the unaerated nappe (see Figure 4(a)). The displacement ( $\Delta x$ ) is correlated to the differential volume of the trapped air behind the nappe. As can be seen from Figure 8, ( $\Delta x$ ) is negative (decreasing in the volume of the trapped air) except for the QRU at unit discharge less than  $q = 20 \times 10^{-3} \text{ m}^2/\text{s}$ . For the QRU and at the unit discharge between  $q = 20 \times 10^{-3} \text{ m}^2/\text{s}$  and  $q = 24 \times 10^{-3} \text{ m}^2/\text{s}$ , the displacement ( $\Delta x$ ) is zero and the nappe is not oscillating for both cases. At unit discharge higher than  $q = 24 \times 10^{-3} \text{ m}^2/\text{s}$ , the displacement ( $\Delta x$ ) becomes negative and the volume of the trapped air decreases causing the nappe to vibrate. For the HR crest, the data for the ( $\Delta x$ ) is not available for the unit discharge less than  $q = 20 \times 10^{-3} \text{ m}^2/\text{s}$  since there is no regular nappe and the water is clinging to the weir downstream side. Note that at higher unit discharge the ( $\Delta x$ ) becomes negative. For the REC crest, the ( $\Delta x$ ) is also negative. It should be noted that there is no nappe vibration observed for all crest shapes at the unit discharge of  $q = 20 \times 10^{-3} \text{ m}^2/\text{s}$  at which the value of ( $\Delta x$ ) is the minimum among the other unit discharges. This means that the change in the displacement

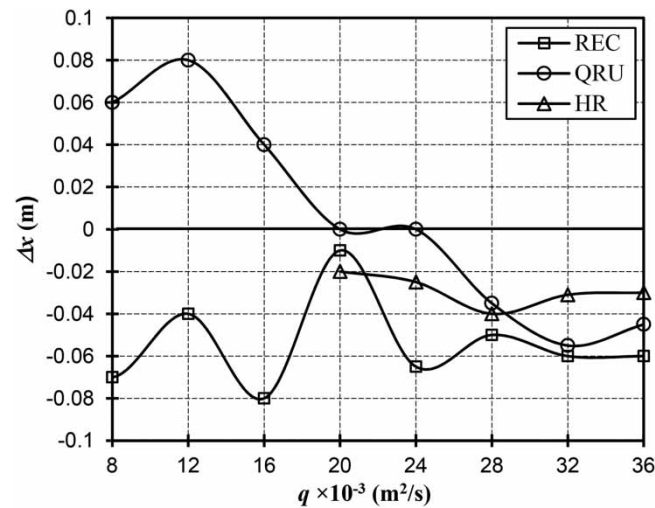


**Figure 8** | The nappe displacement ( $\Delta x$ ) as a function of the unit discharge for different weir crest shapes.

of ( $\Delta x$ ), which is related to the trapped air volume, is very essential for the oscillation to take place. Also, note that the relationship between ( $\Delta x$ ) and the unit discharge is random.

### Time-averaged velocity profiles

Velocity field measurements are collected for the flow field over the weir crest for different crest shapes using the PIV techniques. The velocity measurements are presented at a location before the nappe leaves the crest where  $x = 0.076$  m for the QRU and REC crests and at  $x = 0.06$  m for QRD and HR.  $u$  and  $v$ -velocity measurements for different weir crests at  $q = 8 \times 10^{-3} \text{ m}^2/\text{s}$  are shown in Figure 9. It can be shown from the data in Figure 9 that the maximum  $u$ -velocity is located near the crest wall rather than near the free surface regardless of the crest type. However, the maximum  $v$ -velocity profiles are located near the crest wall for the QRD and HR crests and near the free surface for the QRU and REC crests. Note that the maximum  $u$ -velocities have a large deviation among the different crest shapes. The QRD crest has the maximum  $u$ -velocity and its nappe is stable. If this criterion is used to determine the stability of the other crest, this is not valid for the HR crest that has the

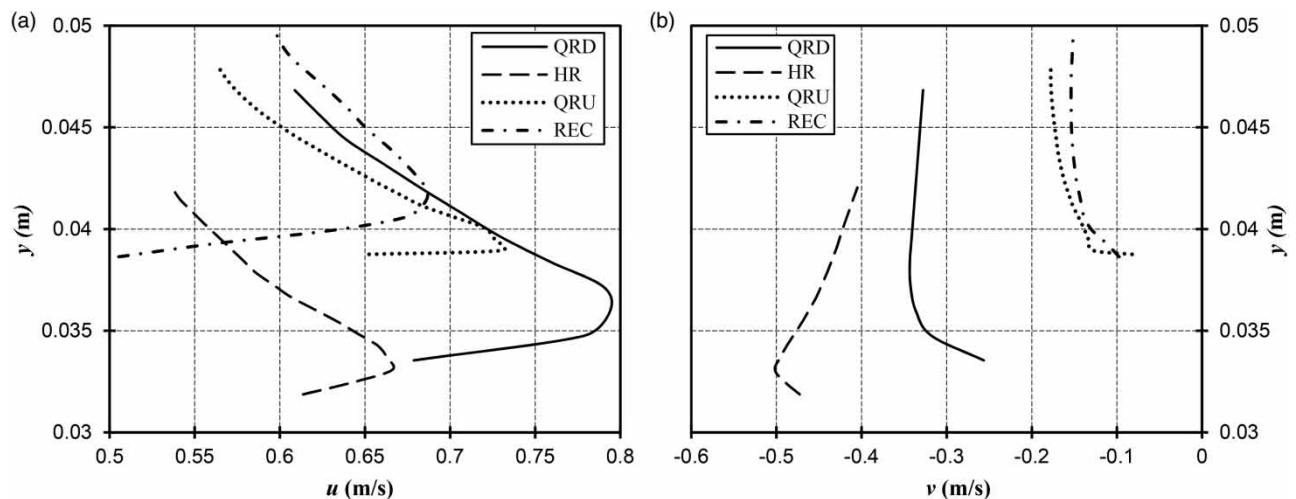


**Figure 9** | Velocities profiles for different weir crests for  $q = 8 \times 10^{-3} \text{ m}^2/\text{s}$  and at a location before the nappe leaves the crest: (a)  $u$ -velocity profiles; (b)  $v$ -velocity profiles.

minimum  $u$ -velocity and has a non-oscillating nappe. For the  $v$ -velocity profiles, the  $v$ -velocity for the HR was the maximum velocity among the other crest shapes and has a stable nappe. The second higher  $v$ -velocity is the QRD which has a stable nappe. The lowest  $v$ -velocity is for the QRU and REC which are unstable. So, the maximum  $v$ -velocity might be used as a criterion for the nappe stability but this is only true at lower flow rates. Figure 10 shows  $u$  and  $v$ -velocities at a unit discharge of  $q = 36 \times 10^{-3} \text{ m}^2/\text{s}$  for different crest shapes. The differences between the  $u$ -velocity profiles are less than that one at lower flow rates and the maximum  $u$ -velocity differences converge. QRD crest still has the maximum  $u$ -velocity and has stable nappe, the second maximum  $u$ -velocity is for HR and QRU crests and they have unstable nappe. The lowest  $u$ -velocity is for the REC and it is supposed to be the most unstable nappe but actually, it is not. For  $v$ -velocity at higher flow rates (Figure 10(b)), the maximum  $v$ -velocity is for the QRD which is stable and the second higher is the HR which is not stable. Thus, from the data shown in Figures 9 and 10, the velocities distributions do not provide a clear picture of the stability of the nappe except that the nappe can be considered stable if the  $v$ -velocity is a higher value relative to that of a stable nappe.

### Weber number (W)

The Weber number can be calculated per the following equation:

$$W = \frac{\rho(\bar{V}_m)^2 d}{\sigma} \quad (2)$$

where  $\rho$  is the water density,  $d$  is the thickness of the nappe,  $\sigma$  is the surface tension, and  $(\bar{V}_m)$  is the average velocity of the water across the nappe. In an effort to investigate the influence of the Weber number on the nappe instability, the Weber number is calculated and plotted for the nappe created with different crest shapes. The Weber number is calculated along the path line (S) located at the center of the nappe as shown in Figure 11. Figure 12 shows the Weber number for different nappe created with different crest shapes as a function of the path line (S) at lower and higher flow rates. It should be noted that the available data for the Weber number is limited by the available velocities collected with the PIV system since it is impossible to collect PIV measurements for a very thin nappe with the current PIV equipment. As shown from the data in Figure 12, the Weber number is proportional to the path line and the Weber number accelerates along the nappe trajectory. Note that the relationship between the Weber number and the path length (S) is approximately linear. De Luca & Costa (1997) and De Luca (1999) found that the nappe transmitted from absolute to convective instability occurs at a location where the Weber number is unity. However, the data in Figure 12 show that the Weber number cannot reach unity at any location of the nappe even at a lower flow rate ( $q = 8 \times 10^{-3} \text{ m}^2/\text{s}$ ) at which the nappe is considered as a thin water

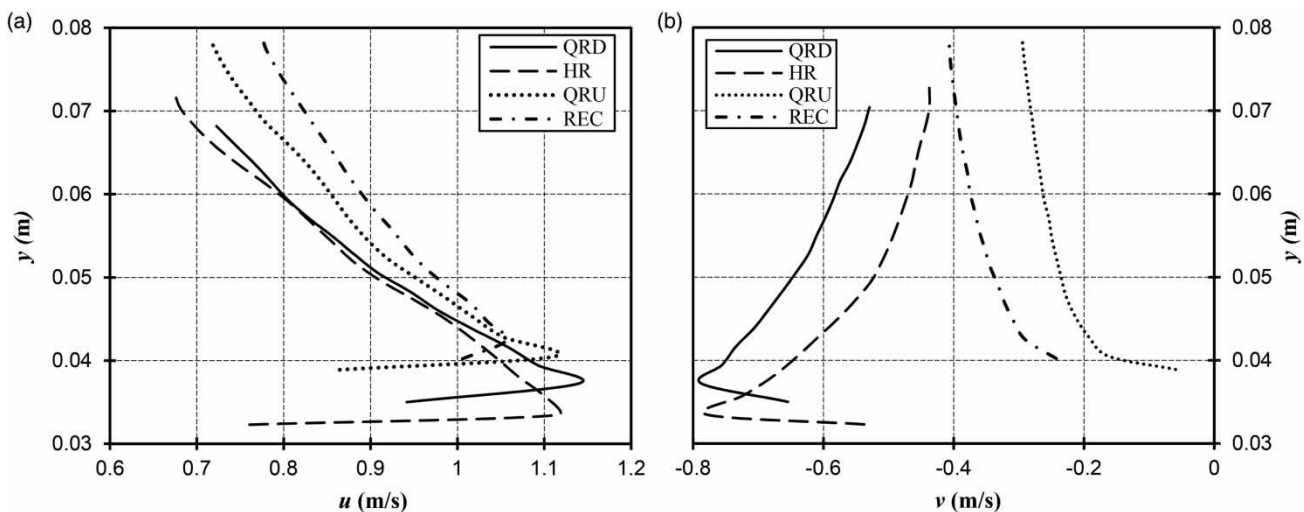


**Figure 10** | Velocities profiles for different weir crests for  $q = 36 \times 10^{-3} \text{ m}^2/\text{s}$  at a location before the nappe leaves the crest: (a)  $u$ -velocity profiles; (b)  $v$ -velocity profiles.

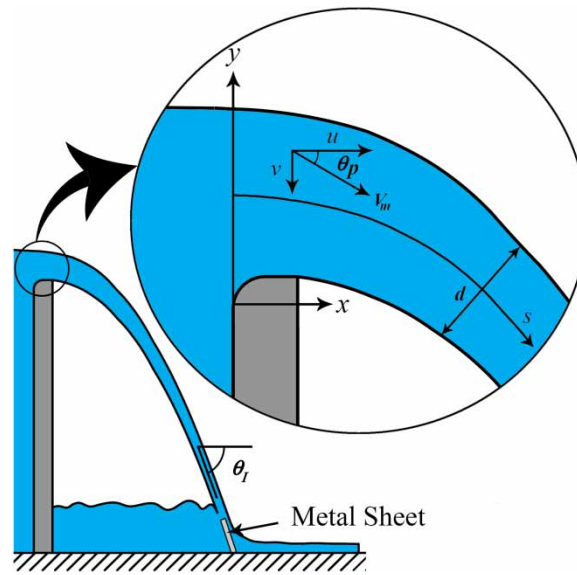


**Figure 11** | Path length and the projection and impact angles.

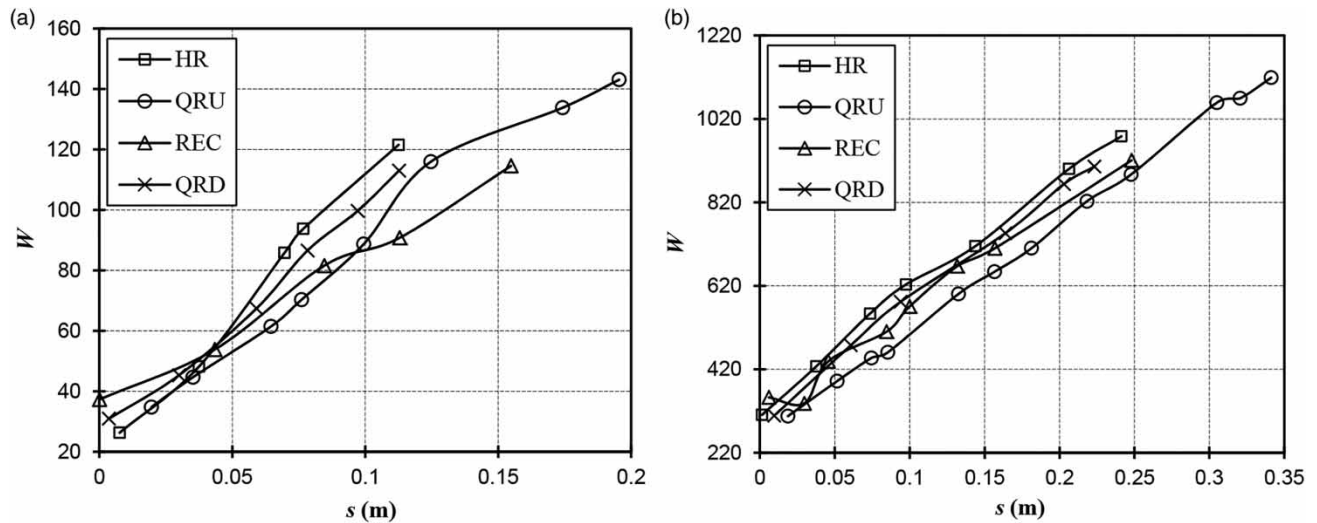


**Figure 12** | Weber number for different weir crest shapes: (a) at  $q = 8 \times 10^{-3} \text{ m}^2/\text{s}$ ; (b)  $q = 36 \times 10^{-3} \text{ m}^2/\text{s}$ .

sheet. Thus, and based on the experimental data used to calculate the Weber number, the Weber number is not a good indicator for the nappe instability.

### Projection and impact angles

Probably the velocity profiles as  $u$  and  $v$  values for the nappe over the weir crest do not provide a clear picture of the nappe instability. But the velocity profiles can provide a better understanding of the nappe instability if they are presented differently. Figure 11 introduces a new parameter that is very important for the nappe instability which is the projection angle ( $\theta_p$ ). As shown in Figure 11, the projection angle is defined as:

$$\theta_p = \tan^{-1} \left( \frac{v}{u} \right) \quad (3)$$

which can be explained as the angle at which the nappe leaves the crest. The average projection angle ( $\overline{\theta_p}$ ) is calculated across

the nappe depth per the following equation:

$$\bar{\theta}_p = \frac{\sum_{i=1}^n \theta_p}{n} \quad (4)$$

where the  $n$  is the number of collected data across the nappe. The average projection angles are shown in Figure 13 at different unit discharges and for different crest shapes before the nappe leaves the crest (at  $x = 0.076$  for QRU and REC and at  $x = 0.06$  for HR and QRD). Before showing the influence of this angle on the nappe instability, it should be noted that when this angle is close to zero degree, the flow is considered horizontal flow and when this angle is close to  $-90$  degrees, the flow is considered vertical. For the unit discharges of  $q < 20 \times 10^{-3} \text{ m}^2/\text{s}$ , the average projection angle is close to zero degree for the nappe produced with REC crest, and then comes QRU, QRD, and HR crest. Note that this order is the same order of the nappe instability for crest shapes, i.e., the nappe created with the REC crest is unstable relative to that one created with QRU, and then comes the HR and QRD crest. Note that the average projection angles for the REC and QRU crests are close to zero compared to the HR and QRD crests. This means that the nappe produced with the REC and QRU crests is more horizontal than that produced with HR and QRD crests. As mentioned before and at the unit discharge of  $q = 20 \times 10^{-3} \text{ m}^2/\text{s}$ , all the nappes created with different crest shapes are stable. The average projection angles for the REC and QRU intersects at a unit flow rate of  $q \cong 21 \times 10^{-3} \text{ m}^2/\text{s}$  and average projection angle of  $-17^\circ$ . This intersection indicates that flows in REC and QRU are hydraulically similar and should have the same nappe oscillation behavior and that what can be found in Table 1 (both are stable). The same intersection exists for HR and QRD crests with an interaction point of  $q \cong 22 \times 10^{-3} \text{ m}^2/\text{s}$  and average projection angle of  $-35^\circ$ . Note that both have the same stable nappe behavior. Also, note that the average projection angles for the REC and QRU crest converge at  $20 \times 10^{-3} < q < 24 \times 10^{-3} \text{ m}^2/\text{s}$  and the nappe is considered stable within this range of the flow rate. This is also true for the HR and QRD crests. At the higher unit discharge of  $q > 24 \times 10^{-3} \text{ m}^2/\text{s}$ , the average of the projection angle for nappe created with the QRU crest becomes closer to zero compared to that one created with the REC crest. The nappe created with the REC crest at higher flow rates is considered more stable relatively compared to the nappe created with the QRU crest. Note that  $(\bar{\theta}_p)$ , the nappe created with the QRU crest, increases as the flow increases when  $q > 24 \times 10^{-3} \text{ m}^2/\text{s}$ , this means that the flow becomes more horizontal. For the HR,  $(\bar{\theta}_p)$  increases as the flow rate increases for  $q > 24 \times 10^{-3} \text{ m}^2/\text{s}$  and that makes the nappe created with this crest become unstable as mentioned before. Note that  $(\bar{\theta}_p)$ , the nappe created with the QRD crest, has the lowest values (most stable one) which is considered less horizontal compared with the other nappes. However,  $(\bar{\theta}_p)$  the QRC crest starts to increase at  $q > 32 \times 10^{-3} \text{ m}^2/\text{s}$ . Based on the data shown in Figure 13, it can be concluded that the nappe is relatively considered as unstable as the average of the projection angle  $(\bar{\theta}_p)$  is more horizontal and vice versa.

The average of the projection angle  $(\bar{\theta}_p)$  has an indirect relationship with another angle called the impact angle  $(\theta_i)$  which is defined as the angle between the nappe stream near the apron and the horizontal as shown in Figure 11. Figure 14 shows the  $(\bar{\theta}_p)$  at  $x = 0.076 \text{ m}$  and  $(\theta_i)$  as a function of the unit discharge for the QRU crest. As mentioned before, the  $(\bar{\theta}_p)$  increases (less

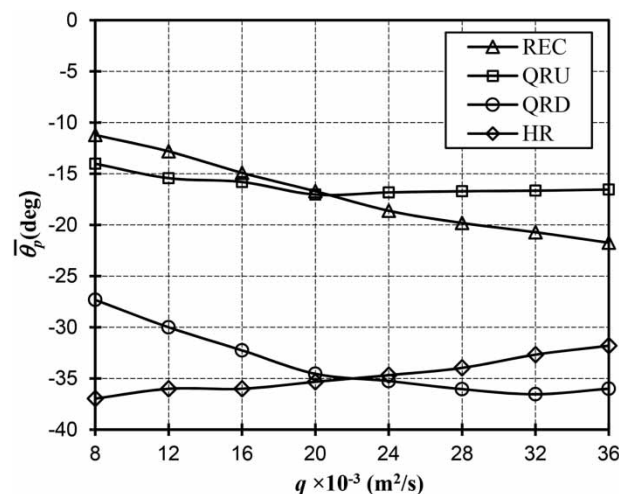


**Figure 13** | The projection angle as a function of unit discharge for different weir crest shapes.



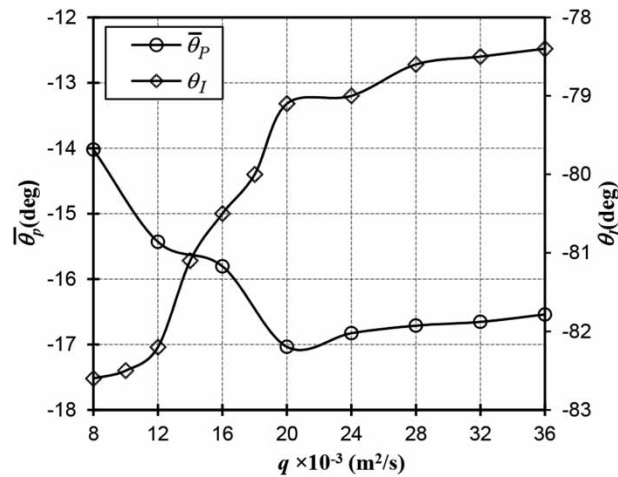


**Figure 14** | The projection angle and the impact angle (at  $x = 0.076 \text{ m}$ ) as a function of unit discharge for QRU.

horizontal) as the flow rate increases until  $q = 20 \times 10^{-3} \text{ m}^2/\text{s}$  after which ( $\bar{\theta}_p$ ) decreases and the flow becomes more horizontal again (less stable). In the meanwhile, ( $\theta_I$ ) decreases as the flow rate increases until it reaches the unit discharges of  $q = 20 \times 10^{-3} \text{ m}^2/\text{s}$  and  $q = 24 \times 10^{-3} \text{ m}^2/\text{s}$  where there is no change in the impact angle and the nappe is considered stable. Then, ( $\theta_I$ ) continues to decrease and the angle moves toward the zero (less stable). Thus, as ( $\theta_I$ ) becomes close to zero ( $\bar{\theta}_p$  is more horizontal), the nappe becomes unstable relative to that nappe with a value of ( $\theta_I$ ) far away from zero.

This angle ( $\theta_I$ ) is one of the most important parameters that can influence the unaerated nappe instability and has a significant effect on the nappe instability mechanism. When the nappe falls under gravity over the weir crest and hits the apron, two regions are created: the trapped region and the ambient region. The trapped region contains the trapped air and trapped water behind the nappe. Whereas, the ambient region contains the tailwater and the ambient air. If the nappe is aerated, the pressure of the trapped air behind the nappe is the same as the pressure of the ambient air. As the nappe hits the water (apron), the lower surface of the nappe mixes some of the trapped air with trapped water and converts the air into air bubbles as shown in Figure 15. In the meanwhile, the outer surface of the nappe mixes some of the ambient air with the tailwater and converts the air into air bubbles. The nappe works as a solid barrier between the two regions (trapped and ambient regions) as long as the nappe doesn't hit the tailwater, but underneath the tailwater and the trapped water surface, the nappe works as a flexible wall that lets the exchange of the air bubbles between the trapped region and the ambient region. So, some of the mixed air bubbles in both regions return into the trapped air or ambient air since the density of the air is less than the density of the water. However, some mixed air bubbles are exchanged between the two regions through the flexible wall. If more of the air bubbles that are mixed from the trapped region are retrained to tailwater and then to the ambient air, a reduction in the pressure behind the nappe will occur and in this case, the nappe performs as a vacuum. The reduction in the pressure causes

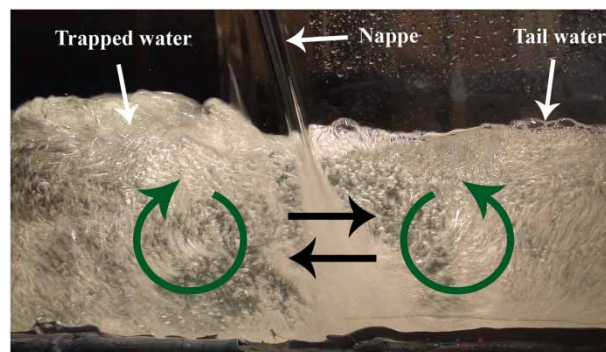


**Figure 15** | Photograph for the air bubbles exchange while the nappe impacts the apron.

the nappe to shift back toward the weir wall as happens in the REC, QRU (at high flow rates), and HR (at high flow rates). If this process continues and the nappe is unaerated, the trapped air pressure dropped down and the pressure difference between the trapped air and the ambient air increases until the nappe cannot afford more reduction in the pressure. At this time, two forces exert on the nappe and work against each other: the differential pressure force which tries to move the nappe back toward the weir wall, and the inertia force that tries to return the nappe to the position when it is fully aerated. When the nappe cannot afford more reduction in the pressure created behind the nappe (unstable nappe), some of the ambient air enters and diffuses into the trapped air through the flexible wall to compensate for the loss in the trapped air. This results in moving the nappe forward slightly and, in this case, the flexible wall acts as a pressure relief valve. This process (moving the ambient air to the trapped air) shuts down immediately since most of the air bubbles that dissolved in the trapped water are more likely to move toward the tailwater. The sudden movement of the ambient air to the trapped air which is interrupted later will cause the first spark for the vibration to occur. As it is well known that the air is a compressible fluid, the air acts as a spring and the nappe starts to move back and forth causing the instability to take place due to the air compressibility. The nappe and the trapped air are similar to the mass-spring system.

If the air bubbles that mixed from the ambient air are retained in the trapped water and then in the trapped air, the pressure of the trapped air will increase and in this case, the nappe performs as a compressor which is similar to that one happen in the nappe created with the QRU at low flow rates. The movement of the air bubbles either to the ambient region or to the trapped region depends on the impact angle ( $\theta_I$ ) which is correlated to the flow rates, crest shapes, and the projection angle. For this reason, the nappe instability is related to the flow rate, i.e. some nappes are more stable than others at different flow rates. The process of entraining the air bubbles to either the trapped region or the ambient region is slow and it takes a long time until the nappe reaches the unstable stage. This explains why the nappe instability doesn't happen frequently. In an effort to prove the proposed theory of nappe instability mechanism, a metal sheet was placed at the impact region as shown in Figure 11 and worked as a solid barrier to prevent the air bubbles exchange between the trapped air and the ambient air. With this installation, neither volume change nor oscillation was observation for originally unstable nappe at the same flow conditions and weir crest shape. There are two effective mitigation techniques that can be used to solve the nappe instability: by venting the nappe or by changing the impact angle ( $\theta_I$ ) and setting the angle in such a way that doesn't let any air bubbles exchange between the trapped and the ambient regions, for example, at  $\theta_I = -79.1^\circ$  for the nappe created with the QRU at the unit discharge of  $q = 20 \times 10^{-3} \text{ m}^2/\text{s}$ . It should be noted that gravity is the driving force to vacuum or compress the trapped air. Also, it should be noted that increasing and decreasing trapped air pressure can be induced manually by charging the trapped air with air using a compressor or by vacuuming the air from the trapped region with a vacuum machine. This will make the nappe unstable and the nappe will vibrate.

## CONCLUSION

The nappe instability was investigated experimentally as a function of flow rate and weir crest shape as well as differential pressure between the trapped region and the ambient air, nappe trajectory profile, velocities profiles, Weber number, nappe projection angle, and the impact angle. There are two types of vibration causes for confined nappes: (a) increasing-pressure increasing-volume and (b) decreasing-pressure decreasing-volume. The later one has relatively harder oscillation behavior. It was found that the increase or the decrease in the pressure of the trapped air was the main reason for the nappe instability of confined nappe. The reduction or increase in the pressure is due to air bubbles exchange between the trapped and the ambient region. The impact angle has a significant effect on the nappe instability because it determines the direction of travel air bubbles. Nappe instability appears to be relatively independent of the Weber number and the nappe velocities profile. Also, the nappe instability varies strongly on crest shape. The REC crest was the most unstable crest at lower discharges, followed by the QRU. The QRU crest was the most unstable crest at higher discharges followed by the REC crest. The HR crest and the QRD crests produced the most stable nappe at lower discharges. But at higher discharges, the HR crest produced unstable nappe. The QRD has the most stable nappe regardless of the flow rates. In general, if the flow leaving the crest is more horizontal, the nappe is more unstable. It can be concluded that the nappe is stable for unit discharge between  $20 \times 10^{-3}$  and  $24 \times 10^{-3} \text{ m}^2/\text{s}$  regardless weir crest shape and the stable projection angle is  $-17^\circ$  (for REC and QRU weirs) and  $-35^\circ$  (for HR and QRD weirs). The stable projection angles mentioned previously are specific for the tested weir elevation.

## ACKNOWLEDGEMENTS

Funding for this study was provided by the State of Utah and the Utah Water Research Laboratory.

## DATA AVAILABILITY STATEMENT

All relevant data are included in the paper or its Supplementary Information.

## CONFLICT OF INTEREST

The authors declare there is no conflict.

## REFERENCES

- Anderson, A. A. 2014 *Causes and Countermeasures for Nappe Oscillation*. Master's Thesis, Utah State University, Logan, UT, USA.
- Anderson, A. & Tullis, B. P. 2018 *Finite crest length weir nappe oscillation*. *Journal of Hydraulic Engineering* **144** (6).
- Barlow, N. S., Helenbrook, B. T. & Lin, S. P. 2010 *Transience to instability in a liquid sheet*. *Journal of Fluid Mechanics* **666**, 358–390.
- Crookston, B. M. & Tullis, B. P. 2012a *Hydraulic design and analysis of labyrinth weirs. I: discharge relationships*. *Journal of Irrigation and Drainage Engineering* **139** (5), 363–370. [https://doi.org/10.1061/\(ASCE\)IR.1943-4774.0000558](https://doi.org/10.1061/(ASCE)IR.1943-4774.0000558).
- Crookston, B. M. & Tullis, B. P. 2012b *Hydraulic design and analysis of labyrinth weirs. II: nappe aeration, instability, and vibration*. *Journal of Irrigation and Drainage Engineering* **139** (5), 371–377. [https://doi.org/10.1061/\(ASCE\)IR.1943-4774.0000553](https://doi.org/10.1061/(ASCE)IR.1943-4774.0000553).
- Crookston, B. M., Anderson, A., Shearin-Feimster, L. & Tullis, B. P. 2014 Mitigation investigation of flow-induced vibrations at a rehabilitated spillway. In *Proc., 5th Int. Symp. on Hydraulic Structures: Hydraulic Structures and Society – Engineering Challenges and Extremes*, University of Queensland, Brisbane, Australia, pp. 149–156. <https://doi.org/10.14264/uql.2014.30>.
- De Luca, L. 1999 *Experimental investigation of the global instability of plane sheet flows*. *Journal of Fluid Mechanics* **399**, 355–376.
- De Luca, L. & Costa, M. 1997 *Instability of a spatially developing liquid sheet*. *Journal of Fluid Mechanics* **331**, 127–144.
- De Rosa, F. 2013 *Dinamiche Instazionarie ed Instabilita' Lineare Globale di Getti Liquidi*. PhD Thesis, Universita' di Napoli Federico II. Available from: <http://www.fedoa.unina.it/9459/>.
- De Rosa, F., Gurfoglio, M. & De Lucac, L. 2014 *Global dynamics analysis of nappe oscillation*. *Physics of Fluids* **26**, 122109.
- Gurfoglio, M., De Rosa, F., Coppola, G. & De Luca, L. 2017 *Unsteady critical liquid sheet flows*. *Journal of Fluid Mechanics* **821**, 219–247.
- Heller, V. 2011 *Scale effects in physical hydraulic engineering models*. *Journal of Hydraulic Research* **49** (3), 293–306. <https://doi.org/10.1080/00221686.2011.578914>.
- Khodier, M. A. & Tullis, B. P. 2017 *PIV measurements for oscillating liquid nappe*. *Journal of Hydro-Environmental Research* **19**, 237–242. <https://doi.org/10.1016/j.jher.2017.11.002>.
- Kitsikoudis, V., Lodomez, M., Dewals, B., Archambeau, P., Pirotton, M. & Erpicum, S. 2021 *Occurrence and characteristic frequencies of nappe*. *Journal of Hydraulic Engineering* **147** (2), 126628. [https://doi.org/10.1061/\(ASCE\)HY.1943-7900.0001839](https://doi.org/10.1061/(ASCE)HY.1943-7900.0001839).
- Kyotoh, H. 2002 Incipient oscillations of a sheet of falling water and the instability mechanisms. *Journal of Hydrosience and Hydraulic Engineering* **20** (1), 77–93.
- Lodomez, M., Pirotton, M., Dewals, B., Archambeau, P. & Erpicum, S. 2016 Frequencies of nappe vibration for free-overfall structures. In *Proc., 6th International Junior Researcher and Engineer Workshop on Hydraulic Structures (IJREWHS)*, Utah State University, Logan, UT, USA.
- Lodomez, M., Dewals, B., Archambeau, P., Pirotton, M. & Erpicum, S. 2018a In-situ measurement and mitigation of nappe oscillations – The Papiognies and Nisramont dams in Belgium. In *Proc., 7th IAHR Int. Symp. on Hydraulic Structures*, Utah State University, Logan, UT, USA.
- Lodomez, M., Pirotton, M., Dewals, B., Archambeau, P. & Erpicum, S. 2018b *Nappe oscillation on free-overfall structures: experimental analysis*. *Journal of Hydraulic Engineering* **144** (3). [https://doi.org/10.1061/\(ASCE\)HY.1943-7900.0001420](https://doi.org/10.1061/(ASCE)HY.1943-7900.0001420).
- Lodomez, M., Crookston, B. M., Tullis, B. P. & Erpicum, S. 2019a *Mitigation techniques for nappe oscillations on free-overfall structures*. *Journal of Hydraulic Engineering* **145** (2). [https://doi.org/10.1061/\(ASCE\)HY.1943-7900.0001558](https://doi.org/10.1061/(ASCE)HY.1943-7900.0001558).
- Lodomez, M., Tullis, B. P., Pirotton, M., Dewals, B., Archambeau, P., Pirotton, M. & Erpicum, S. 2019b *Nappe oscillations on free-overfall structures: size scale effects*. *Journal of Hydraulic Engineering* **145** (6). [https://doi.org/10.1061/\(ASCE\)HY.1943-7900.0001615](https://doi.org/10.1061/(ASCE)HY.1943-7900.0001615).
- Mori, H., Nagamine, T., Ito, R. & Sato, Y. 2012 *Mechanism of self-excited vibration of a falling water sheet*. *Nihon Kikai Gakkai Ronbunshu, C Hen/Transactions of the Japan Society of Mechanical Engineers, Part C* **78** (792), 2720–2732. <https://doi.org/10.1299/kikaic.78.2720>.
- Sato, Y., Miura, S., Nagamine, T., Morii, S. & Ohkubo, S. 2007 *Behavior of a falling water sheet*. *Journal of Environmental Engineering* **2** (2), 394–406.
- Scarano, F. & Riethmuller, M. L. 1999 *Iterative multigrid approach in PIV image processing with discrete window offset*. *Experiments in Fluids* **26** (6), 513–523.
- Schmid, P. J. & Henningson, D. S. 2002 *On the stability of a falling liquid curtain*. *Journal of Fluid Mechanics* **463**, 163–171.

First received 9 May 2022; accepted in revised form 27 August 2022. Available online 5 September 2022